Large- and Small-Signal Average-Value Modeling of Dual-Active-Bridge DC–DC Converter Considering Power Losses

Kai Zhang, Zhenyu Shan, *Member, IEEE*, and Juri Jatskevich, *Senior Member, IEEE*

***Abstract*—Average-value modeling (AVM) provides an efficient way to study power electronic systems in large- and small-signal senses. This paper presents a new reduced-order AVM for dual-active-bridge dc–dc converters. The proposed model considers the conduction and transformer power losses as well as the input/output filters, which may be very useful for system-level studies. Based on the large-signal AVM, the small-signal model and the control-to-output transfer function are also derived. The proposed AVM is compared with the full-order generalized average model and the detailed model in predicting large-signal transients and small-signal analysis in the frequency domain. The experimental results confirm that the proposed model yields a high accuracy, which represents an improvement over other existing models.**

***Index Terms*—Average-value modeling, dual-active-bridge (DAB) converter, power loss estimation, reduced-order model, small-signal analysis.**

I. Introduction

IT is envisioned that dc systems will be used more often in the future in combination with the traditional ac systems in order to increase the power density and reduce the number of conversion stages and energy loss. In the dc power system, which includes dc energy sources and loads, a backup battery with a high-performance bidirectional converter for power management is needed to enhance the system reliability. In some applications, the galvanic isolation may also be required to separate the primary (input) and secondary (output) sides.

There are various topologies of isolated bidirectional dc–dc converters. Most prominent topologies include isolated bidirectional full-bridge converters [1], bidirectional current doubler converters [2], and dual-active-bridge (DAB) converters [3]–[5]. For the application of battery power management, the DAB converter is a good candidate, since it is can offer bidirectional energy flow, inherent soft switching, high-power-density and high-efficiency voltage conversion, and galvanic isolation [3], [6]. In addition, this topology has been widely used in solid-state transformers [7], [8], smart grid applications [9], [10], electric/hybrid vehicles [11], etc. The comprehensive analysis of DAB converters in terms of design, operation, and control may be found in [12] and [13]. Furthermore, recent achievements on DAB converters include the design optimization [13], the advanced control strategies [14], [15], the detailed modeling for power-loss evaluations [11], the generalized average modeling [16], the modeling for rms and average currents of devices [17], and the pulse width modulation (PWM) control [18].

Modeling and simulations of DAB converters can be extremely useful prior to hardware implementations as they help component selection, controller design, and preliminary evaluation of the overall dc system. The detailed switching models may be readily developed in commercial transient simulators. Such models are typically based on parameters of actual components (resistors, inductors, capacitors, diodes, transistors, etc.), which may also include some parasitics (equivalent series resistances, on-conduction resistances of diodes and transistors, forward voltage drops, leakage inductances, etc.) for increasing the simulation accuracy. However, this type of simulation may be time-consuming due to the existence of switching actions, input/output filters, and high-frequency transformers [19]. To reduce the computation effort and gain additional system-level information, the so-called average-value-modeling (AVM) methods have been widely used in the literature. The AVMs are also very useful for investigations of system transients and stability [20]. However, recent works on DAB converters suggest that the nonlinear effect of this circuit is a great obstacle to the development of accurate AVMs [5], [21].

The small-signal ac model of a DAB converter may be attained using the corresponding equivalent average circuits [22], [23]. The conventional state-space averaging method [24] may be used to derive the small-signal transfer function of most converters [25]. However, in the DAB converter, the transformer current has a dominant ac component, which makes it difficult to apply the conventional state-space averaging method. In previous literature, there are two approaches to the average modeling of DAB converters. The first one is to eliminate the switching-frequency ac component of the transformer current and then reduce the order of state variables [26]–[30]. However, power losses are not considered during this procedure. The second approach consists of increasing the state-variable order and extracting the transient component of the transformer current to form a full-order model, either in discrete time [23], [31] or continuous time [16]. Specifically, in the continuous full-order

Manuscript received August 16, 2015; revised February 12, 2016; accepted April 5, 2016. Date of publication April 21, 2016; date of current version December 9, 2016. This work was supported by the Natural Science and Engineering Research Council of Canada, and also by the National Natural Science Foundation of China under Grant 51477144. Recommended for publication by Associate Editor R. Ayyanar.

K. Zhang was with the Department of Electrical and Computer Engineering, University of British Columbia, Vancouver, BC V6T 1Z4 Canada. He is now with Guangzhou Power Supply Co. Ltd., China Southern Power Grid Co. Ltd., Guangzhou 510623, China. (e-mail: kzhang@ece.ubc.ca).

Z. Shan and J. Jatskevich are with the Department of Electrical and Computer Engineering, University of British Columbia, Vancouver, BC V6T 1Z4 Canada (e-mail: zhenyus@ece.ubc.ca; jurij@ece.ubc.ca).

Color versions of one or more of the figures in this paper are available online at http://ieeexplore.ieee.org.

Digital Object Identifier 10.1109/TPEL.2016.2555929

TABLE I
PROPERTIES OF DIFFERENT AVERAGE MODELS FOR DAB CONVERTERS

Models Properties	Conduction loss	Core loss	Leakage inductance	Magnetizing inductance	Model order	Accuracy of predicting steady-state operating points	Accuracy of open-loop dynamic response	Frequency response
Discrete-time full-order model in [23] and [31]	√		√		Full	No discussion in [23], [31]	No discussion in [31]	Accurate up to 1/10 of switching frequency [23]; accurate up to 1/3 of switching frequency [31]
Continuous-time full-order model in [16]	√		√		Full	Low	Low	Accurate up to 1/3 of switching frequency [16]
Reduced-order model without power losses in [27] and [28]			√		Reduced	Low	Low	Low accuracy at low frequency
Proposed reduced-order model	√	√	√	√	Reduced	High	High	Accurate up to 1/10 of switching frequency, especially at low frequency

model, the real and imaginary parts of the transformer current are used as state variables which increase the equation order [16]. In general, a full-order model should be capable of achieving higher accuracy than a reduced-order model [31]. However, the full-order model derived by generalized average modeling is based on the first harmonic only, which implies that its accuracy may suffer when large harmonic distortions are present [32]. In fact, the steady-state error from the generalized average modeling may be substantial [33].

Some of the most relevant previously established average models for DAB converters are tabulated in Table I. Specifically, the discrete-time full-order model in [23] and [31] and the continuous-time full-order model in [16] are built considering the conduction loss and can accurately predict the frequency response.

However, the models in [23] and [31] are presented without direct discussions on the steady-state predictions; the model in [16] has a low accuracy in the prediction of steady-state operating points because only the fundamental-frequency component is considered in the model. The reduced-order model presented in [27] and [28] does not include conduction loss and therefore has low accuracy, as reported in [16]. The advantage of this model is the decreased computations due to its simplified formulation and a small number of state variables.

In this paper, a new reduced-order AVM for DAB converters is proposed. The small-signal transfer function is derived from the proposed model. The property of the new model and the contributions of this paper may be summarized as follows:

1) The proposed model considers all major power losses in the circuit (i.e., conduction loss and core loss). Specifically, the new model considers the equivalent shunt resistance (to represent the transformer core loss), the transformer windings' equivalent series resistance, and switches' (transistors') on resistance, which are not considered in previous reduced-order models [27], [28] but essential for predicting the power losses and the efficiency of converter circuits for system-level studies.

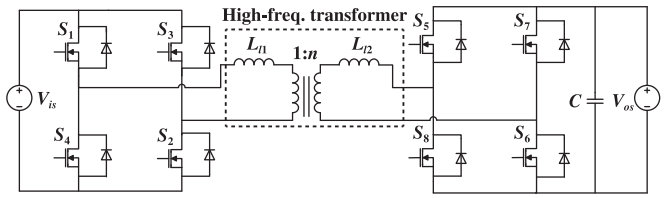

Fig. 1. Topology of a general DAB converter depicting an input bridge, a transformer with leakage inductances, and an output bridge.

2) The new model is formulated as a continuous-time average circuit model with dependent sources, which has a very simple and easy-to-use structure. Moreover, the small-signal ac circuit model has the same structure.
3) The small-signal model is derived from the proposed large-signal AVM model using linearization and the Taylor series approach. Due to inclusion of losses, the prediction of the frequency response obtained from the proposed small-signal model is more accurate than that from the model in [27], [28] for the low-frequency range. For the high-frequency range, the accuracy of the proposed reduced-order model is very close to that of the existing full-order models [16], [23], [31].
4) We present extensive studies and comparisons with detailed simulations, alternative existing models, and experimental measurements to demonstrate that the proposed model is able to accurately predict the steady-state and transient responses, as well as offer a high accuracy in the prediction of the frequency response.

II. DETAILED MODELING OF DAB CONVERTERS

The circuit diagram of a general DAB converter considered in this paper is shown in Fig. 1. The converter consists of a high-frequency transformer (with turns ratio 1: n) and two active bridges: one on the input (primary) side and the other on the output (secondary) side. The transformer provides galvanic isolation and energy delivery through its windings.

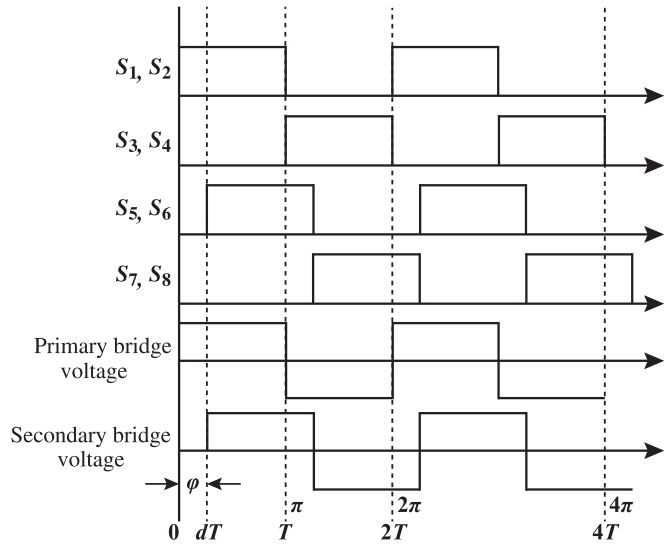

Fig. 2. Simplified diagram of switching signals and transformer voltages.

This paper considers a simple phase shift modulation (PSM) used to control the energy delivery between the input (primary) side and the output (secondary) side. According to the operating principles of PSM, the primary and secondary bridges generate the square-wave voltages with a 50% duty, and the phase shift between the driving signals for the two bridges determines the power level. The MOSFET gate signals and the bridge voltages are shown in Fig. 2. If an ideal transformer is assumed (no power loss is considered), the power delivered from the leading bridge to the lagging bridge may be calculated by

$$P = \frac{V_{is} V_{os}}{2n f_s L_{eq}} d\,(1-d) \tag{1}$$

where n is the turns ratio of the high-frequency transformer, V_{is} and V_{os} are the converter input and output voltages, respectively, $d = \varphi/\pi$ is the phase shift ratio, f_s is the switching frequency, and $L_{eq} = L_{l1} + L_{l2}/n^2$ is the leakage inductance referred to the input side.

In addition to the general DAB shown in Fig. 1, this paper also considers the input/output filters as shown in Fig. 3. These filters are designed as typical LC structures with RC damping branches to suppress the current and voltage ripples. Also, the transformer magnetizing inductance L_M, the equivalent resistance representing the core loss R_M, the leakage inductances L_{l1} and L_{l2}, the winding resistances R_{l1} and R_{l2}, and the turn-on resistance R_s of the MOSFETs are considered. The resistances R_s, R_{l1}, and R_{l2} can be lumped and referred to the primary side as an equivalent resistance, namely

$$R_{eq} = R_{l1} + 2R_s + \frac{R_{l2} + 2R_s}{n^2} \tag{2}$$

since R_M is much greater than R_s, R_{l1}, and R_{l2}. Similarly, lumping the leakage inductances L_{l1} and L_{l2} may yield an equivalent leakage inductance at the primary side, namely

$$L_{eq} = L_{l1} + \frac{L_{l2}}{n^2} \tag{3}$$

since L_M is much greater than L_{l1} and L_{l2}. Taking into consideration (2) and (3), the equivalent detailed circuit model is obtained with R_{eq} and L_{eq}, as shown in Fig. 4.

III. AVM of DAB Converters

A. State Equations of DAB-Converter Steady State

As shown in Fig. 4, the converter circuit can be divided into three subcircuits. Subcircuits I and III can be described by the following equations:

$$L_1 \frac{di_1}{d\tau} = v_{is} - v_{c1} \tag{4}$$

$$L_2 \frac{di_2}{d\tau} = v_{c3} - v_{os} - i_2 R_o \tag{5}$$

$$C_2 \frac{dv_{c2}}{d\tau} = \frac{v_{c1} - v_{c2}}{R_1} \tag{6}$$

$$C_4 \frac{dv_{c4}}{d\tau} = \frac{v_{c3} - v_{c4}}{R_2} \tag{7}$$

$$C_1 \frac{dv_{c1}}{d\tau} = i_1 - i_{aci} - \frac{v_{c1} - v_{c2}}{R_1} \tag{8}$$

$$C_3 \frac{dv_{c3}}{d\tau} = i_{aco} - i_2 - \frac{v_{c3} - v_{c4}}{R_2} \tag{9}$$

where v_{c1}, v_{c2}, v_{c3}, and v_{c4} are voltages across capacitors C_1, C_2, C_3, and C_4, respectively; i_{aci} and i_{aco} are average values of input and output currents corresponding to Subcircuit II, respectively; and τ is used to denote time. The input/output currents (i_{aci} and i_{aco}) include substantial periodic variations, as shown in Fig. 5. Instead of the instantaneous values, the average values are used in the AVM.

It is noted that the period T in Fig. 5 is a half of the switching period. Due to the existence of R_{eq}, the actual curve of i_{aci} and ni_{aco} waveforms are piecewise exponentials (not piecewise linear). Assuming that the currents of the magnetizing inductance and resistance (L_M and R_M) are negligible, i_{aci} can be formulated as follows:

$$i_{aci} = \begin{cases} i_\alpha = \dfrac{v_{c1} + v'_{c3}}{R_{eq}} + \left(-I_{t1} - \dfrac{v_{c1} + v'_{c3}}{R_{eq}}\right) e^{-\frac{R_{eq}}{L_{eq}}\tau}, \\ \qquad\qquad \text{for } (0 \le \tau < dT) \\ i_\beta = \dfrac{v_{c1} - v'_{c3}}{R_{eq}} + \left(I_{t2} - \dfrac{v_{c1} - v'_{c3}}{R_{eq}}\right) e^{-\frac{R_{eq}}{L_{eq}}(\tau - dT)}, \\ \qquad\qquad \text{for } (dT \le \tau < T) \end{cases} \tag{10}$$

where $v'_{c3} = v_{c3}/n$; I_{t1} and I_{t2} are the peak values of the transformer current. It is further assumed that the ripples on v_{c1} and v_{c3} are sufficiently small, and then, v_{c1} and v_{c3} may be assumed constant over the duration T.

Further analyzing Fig. 5, the current values at time instants of 0, dT, and T are, respectively, denoted as $-I_{t1}$, I_{t2}, and I_{t1}, i.e.,

$$i_{aci}(0) = -I_{t1} \tag{11}$$

$$i_{aci}(dT) = I_{t2} \tag{12}$$

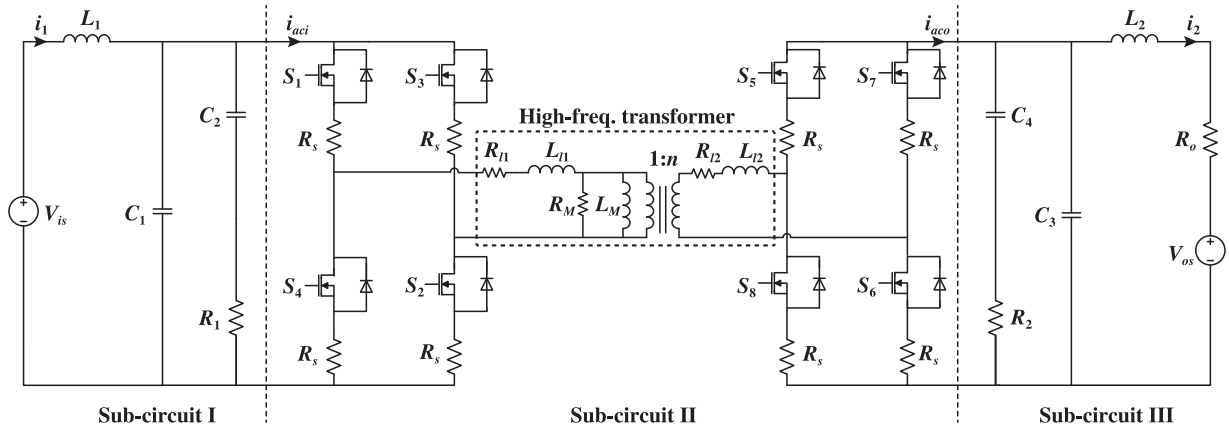

Fig. 3. Detailed circuit model of a DAB converter interfacing input and output sources V_{is} and V_{os}. The circuit includes the leakage inductances L_{l1} and L_{l2}, winding resistances R_{l1} and R_{l2}, magnetizing inductance L_M, core losses equivalent resistance R_M, and MOSFET turn-on resistance R_s.

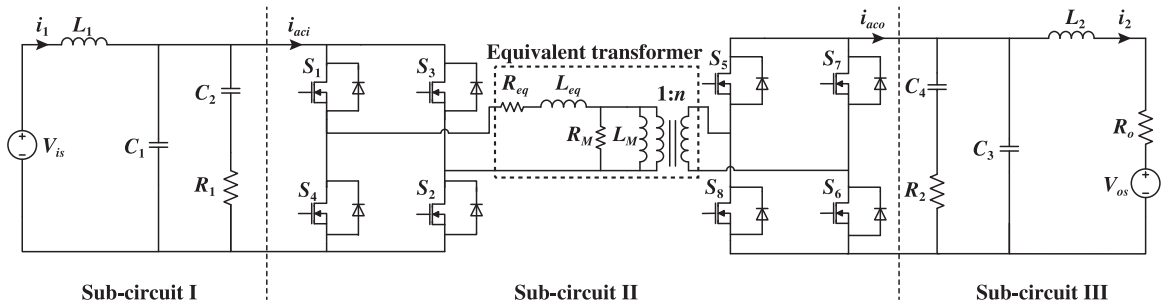

Fig. 4. Equivalent detailed model of the DAB converter with R_{eq} and L_{eq}.

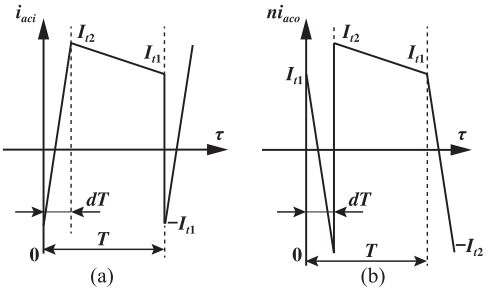

Fig. 5. Transformer input and output currents i_{aci} (a) and ni_{aco} (b) in a half switching period. The values of transformer current peaks are denoted by I_{t1} and I_{t2}.

and

$$i_{aci}(T) = I_{t1}. \tag{13}$$

Referring to (10)–(13), I_{t1} and I_{t2} can be derived as

$$I_{t1} = \frac{\frac{v_{c1}-v'_{c3}}{R_{eq}} + \frac{2v'_{c3}}{R_{eq}} e^{-\frac{R_{eq}}{L_{eq}}(T-dT)} - \frac{v_{c1}+v'_{c3}}{R_{eq}} e^{-\frac{R_{eq}}{L_{eq}}T}}{1+e^{-\frac{R_{eq}}{L_{eq}}T}} \tag{14}$$

and

$$I_{t2} = \frac{\frac{v_{c1}+v'_{c3}}{R_{eq}} - \frac{2v_{c1}}{R_{eq}} e^{-\frac{R_{eq}}{L_{eq}}dT} + \frac{v_{c1}-v'_{c3}}{R_{eq}} e^{-\frac{R_{eq}}{L_{eq}}T}}{1+e^{-\frac{R_{eq}}{L_{eq}}T}}. \tag{15}$$

Note that the waveforms of i_{aci} and $n \cdot i_{aco}$ from 0 to dT are symmetrical about the horizontal axis. Therefore, the average values of i_{aci} and $n \cdot i_{aco}$ for the period T have the form

$$i_{aci} = \frac{1}{T}\left(\int_0^{dT} i_\alpha d\tau + \int_{dT}^{T} i_\beta d\tau\right) \tag{16}$$

and

$$n \cdot i_{aco} = \frac{1}{T}\left[\int_0^{dT} (-i_\alpha)\, d\tau + \int_{dT}^{T} i_\beta d\tau\right] \tag{17}$$

respectively. Substitutions of (10) into (16) and (17) yield

$$\begin{aligned} T \cdot i_{aci} = {} & \frac{v_{c1}+v'_{c3}}{R_{eq}} dT + \frac{v_{c1}-v'_{c3}}{R_{eq}} (1-d)\, T \\ & + \frac{L_{eq}}{R_{eq}} \left(I_{t1} + \frac{v_{c1}+v'_{c3}}{R_{eq}}\right)\left(e^{-\frac{R_{eq}}{L_{eq}}dT} - 1\right) \\ & + \frac{L_{eq}}{R_{eq}} \left(\frac{v_{c1}-v'_{c3}}{R_{eq}} - I_{t2}\right)\left[e^{-\frac{R_{eq}}{L_{eq}}(T-dT)} - 1\right] \end{aligned} \tag{18}$$

and

$$T \cdot n \cdot i_{aco} = -\frac{v_{c1}+v'_{c3}}{R_{eq}}dT + \frac{v_{c1}-v'_{c3}}{R_{eq}}(1-d)\,T - \frac{L_{eq}}{R_{eq}}\left(I_{t1}+\frac{v_{c1}+v'_{c3}}{R_{eq}}\right)\left(e^{-\frac{R_{eq}}{L_{eq}}dT}-1\right) + \frac{L_{eq}}{R_{eq}}\left(\frac{v_{c1}-v'_{c3}}{R_{eq}}-I_{t2}\right)\left[e^{-\frac{R_{eq}}{L_{eq}}(T-dT)}-1\right]. \tag{19}$$

Therefore, (4)–(9), (14), (15), (18), and (19) constitute the reduced-order AVM without core losses or magnetizing inductance.

B. Effect of Magnetizing Inductance and Core Losses

In the model defined by (4)–(9), (14), (15), (18), and (19), the magnetizing current through L_M and the current through R_M are not considered. Actually, the elements L_M and R_M will draw a low current from the power source. In addition, the magnetizing and demagnetizing of the inductor L_M is synchronous with the commutation of bridges, and the period of which is $2T$. Therefore, the averaging of i_{aco} should be taken in $2T$, and (17) is modified as

$$n \cdot i_{aco} = \frac{1}{2T}\left[2\int_0^{dT}(-i_\alpha)\,d\tau + 2\int_{dT}^{T} i_\beta d\tau\right] - \frac{1}{2T}\int_0^{2T} i_M\,d\tau - \frac{v_{c3}}{n\cdot R_M} \tag{20}$$

where i_M is the current in L_M. Moreover, the one-period integral of i_M in steady state should be zero, i.e.,

$$\int_0^{2T} i_M\,d\tau = 0. \tag{21}$$

Therefore, the existence of L_M will not affect the modeling of DAB converters, and (20) may be further simplified as

$$n \cdot i_{aco} = \frac{1}{T}\left[\int_0^{dT}(-i_\alpha)\,d\tau + \int_{dT}^{T} i_\beta d\tau\right] - \frac{v_{c3}}{n\cdot R_M}. \tag{22}$$

The reduced-order AVM with core losses and magnetizing inductance is defined by (4)–(9), (14), (15), (18), (19), and (22). This sixth-order model is referred to as the reduced-order average-value model (RAVM) in this paper. Note that, in this work, the RAVM is proposed for a DAB converter operating with PSM. However, in many applications, the combination of PSM and PWM is used [34], [35]. In this case, the expression of i_{aci} differing from (10) should be rederived. Nevertheless, the analysis approach used in this study is still applicable to the RAVM derivation when different modulation schemes are used.

C. AVM Circuit of DAB

The proposed RAVM circuit is shown in Fig. 6, where the variable values are referred to (4)–(9), (14), (15), (18), and (22). Here, the currents i_{aci} and $n \cdot i_{aco}$ are represented as dependent current sources, and the transformer is treated as an ideal dc transformer (to scale variables). Since there are no switching components in the proposed RAVM, its implementation and simulation will be much faster than that of the detailed model. Also, the small-signal model and the frequency-domain analysis can be readily obtained by linearization.

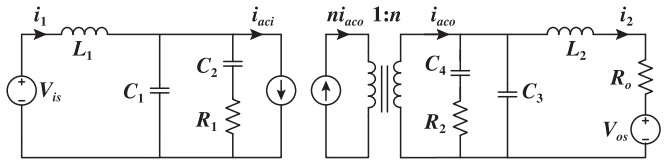

Fig. 6. DAB converter average circuit model, where the currents i_{aci} and ni_{aco} are dependent current sources which are the functions of v_{c1}, v_{c3}, and d.

IV. Small-Signal Model of DAB

To construct a small-signal ac model at a dc operating point, the variables v_{is}, v_{os}, and d are assumed to be equal to their quiescent values plus respective superimposed small ac perturbations, i.e.,

$$v_{is} = V_{is} + \hat{v}_{is} \tag{23}$$

$$v_{os} = V_{os} + \hat{v}_{os} \tag{24}$$

$$d = D + \hat{d}. \tag{25}$$

The output averaged variables i_1, i_2, v_{c1}, v_{c2}, v_{c3}, and v_{c4} will also be equal to their corresponding quiescent values plus respective superimposed small ac variations [25], i.e.,

$$i_1 = I_1 + \hat{i}_1 \tag{26}$$

$$i_2 = I_2 + \hat{i}_2 \tag{27}$$

$$v_{c1} = V_{c1} + \hat{v}_{c1} \tag{28}$$

$$v_{c2} = V_{c2} + \hat{v}_{c2} \tag{29}$$

$$v_{c3} = V_{c3} + \hat{v}_{c3} \tag{30}$$

$$v_{c4} = V_{c4} + \hat{v}_{c4}. \tag{31}$$

The small-signal model can be derived by substituting (23) into (31) into the previous large-signal average model. In this process, the dc terms will be eliminated, and the second- and higher order ac terms will be neglected.

Noting that during this derivation process, there will be equations with terms $e^{a\hat{d}}$, where a is a constant coefficient. According to Taylor series, when $\hat{d}$ is close enough to zero, the terms $e^{a\hat{d}}$ can be expressed as an infinite convergent series

$$e^{a\hat{d}} = \sum_{n=0}^{\infty}\frac{\left(a\hat{d}\right)^n}{n!} = 1 + \frac{a}{1!}\hat{d} + \frac{a^2}{2!}\hat{d}^2 + \cdots + \frac{a^n}{n!}\hat{d}^n + \cdots. \tag{32}$$

If the second- and higher order terms are ignored, $e^{a\hat{d}}$ will be approximated as

$$e^{a\hat{d}} = 1 + a\hat{d}. \tag{33}$$

When (33) is utilized to linearize the average model at a certain operating point, the resulting small-signal model can be

formulated as follows:

$$L_1\frac{d\hat{i}_1}{d\tau} = \hat{v}_{is} - \hat{v}_{c1} \tag{34}$$

$$L_2\frac{d\hat{i}_2}{d\tau} = \hat{v}_{c3} - \hat{v}_{os} - \hat{i}_2 R_o \tag{35}$$

$$C_2\frac{d\hat{v}_{c2}}{d\tau} = \frac{\hat{v}_{c1} - \hat{v}_{c2}}{R_1} \tag{36}$$

$$C_4\frac{d\hat{v}_{c4}}{d\tau} = \frac{\hat{v}_{c3} - \hat{v}_{c4}}{R_2} \tag{37}$$

$$C_1\frac{d\hat{v}_{c1}}{d\tau} = \hat{i}_1 - \hat{i}_{aci} - \frac{\hat{v}_{c1} - \hat{v}_{c2}}{R_1} \tag{38}$$

$$C_3\frac{d\hat{v}_{c3}}{d\tau} = \hat{i}_{aco} - \hat{i}_2 - \frac{\hat{v}_{c3} - \hat{v}_{c4}}{R_2} \tag{39}$$

where

$$\hat{i}_{aci} = p\hat{d} + q\hat{v}_{c1} + r\hat{v}_{c3} \tag{40}$$

$$n\cdot\hat{i}_{aco} = x\hat{d} + y\hat{v}_{c1} + z\hat{v}_{c3}. \tag{41}$$

Here, the variables p, q, r, x, y, and z are defined as

$$p = \frac{2V_{c3}}{nR_{eq}} - \frac{4e^{-\frac{R_{eq}}{L_{eq}}(1-D)T}}{R_{eq}\left(e^{-\frac{R_{eq}}{L_{eq}}T}+1\right)}\cdot\frac{V_{c3}}{n} \tag{42}$$

$$q = \frac{1}{R_{eq}} + \frac{1}{T}\cdot\frac{L_{eq}}{R_{eq}}\cdot\frac{2\left(e^{-\frac{R_{eq}}{L_{eq}}T}-1\right)}{R_{eq}\left(e^{-\frac{R_{eq}}{L_{eq}}T}+1\right)} \tag{43}$$

$$r = \frac{1}{n}\cdot\frac{2D-1}{R_{eq}} + \frac{1}{n}\cdot\frac{1}{T}\cdot\frac{L_{eq}}{R_{eq}}\cdot\frac{2\left[e^{-\frac{R_{eq}}{L_{eq}}T} - 2e^{-\frac{R_{eq}}{L_{eq}}(1-D)T}+1\right]}{R_{eq}\left(e^{-\frac{R_{eq}}{L_{eq}}T}+1\right)} \tag{44}$$

$$x = \frac{-2V_{c1}}{R_{eq}} + \frac{4e^{-\frac{R_{eq}}{L_{eq}}DT}}{R_{eq}\left(e^{-\frac{R_{eq}}{L_{eq}}T}+1\right)}\cdot V_{c1}, \tag{45}$$

$$y = \frac{1-2D}{R_{eq}} + \frac{1}{T}\cdot\frac{L_{eq}}{R_{eq}}\cdot\frac{2\left(e^{-\frac{R_{eq}}{L_{eq}}T} - 2e^{-\frac{R_{eq}}{L_{eq}}DT}+1\right)}{R_{eq}\left(e^{-\frac{R_{eq}}{L_{eq}}T}+1\right)} \tag{46}$$

$$z = \frac{1}{n}\left[-\frac{1}{R_{eq}} + \frac{1}{T}\cdot\frac{L_{eq}}{R_{eq}}\cdot\frac{2\left(1-e^{-\frac{R_{eq}}{L_{eq}}T}\right)}{R_{eq}\left(1+e^{-\frac{R_{eq}}{L_{eq}}T}\right)} - \frac{1}{R_M}\right] \tag{47}$$

Based on derivations in (23)–(47), the small-signal ac circuit model of DAB converters is constructed in the same way as the proposed large-signal model shown in Fig. 6. Specifically, the same circuit of Fig. 6 is used, wherein the corresponding variables are replaced with their small-signal definitions (23)–(31), and the input- and output-dependent current sources are replaced by (40) and (41), respectively.

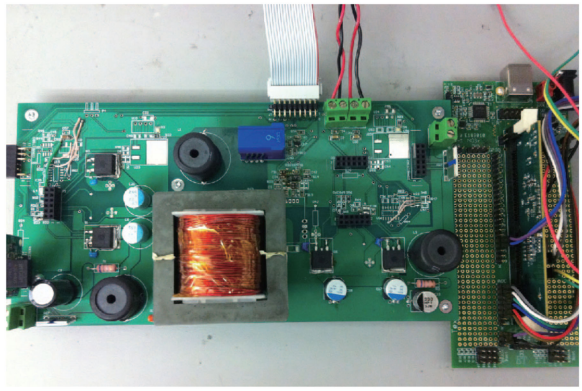

Fig. 7. Photo of the experimental DAB converter.

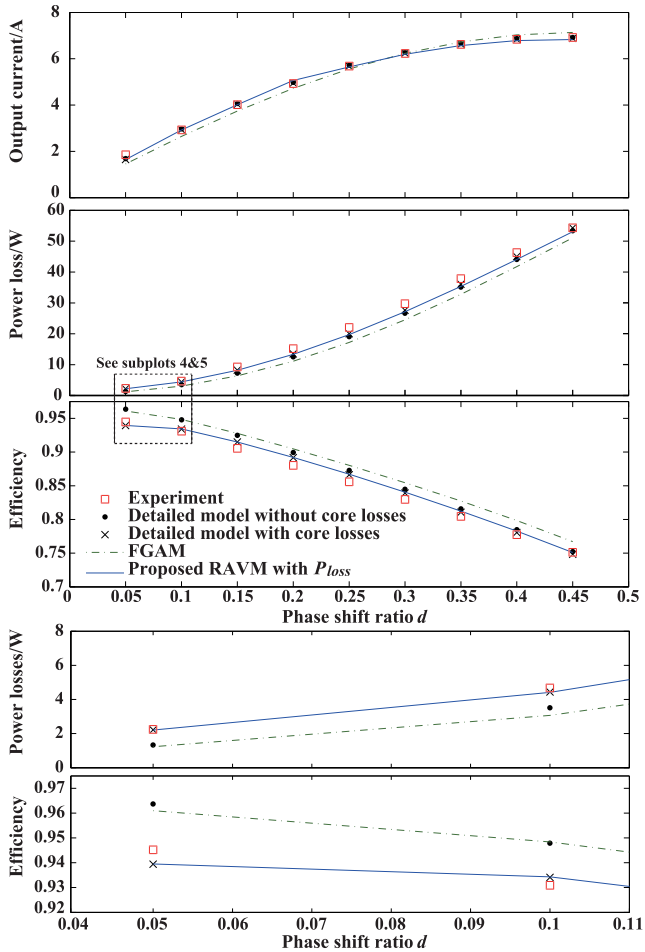

Fig. 8. Output current, power losses, and efficiency predictions compared to the actual measurements, with $V_{is} = 48$ V and $V_{os} = 20$ V. Results are from the experimental measurement (square markers), the detailed model without core losses (dot markers), the detailed model with core losses (cross markers), FGAM (dash-dotted line), and the proposed RAVM with power losses (solid line).

The frequency-domain analysis may also be carried out using linearization and subsequent calculations of various transfer functions. If the Laplace transform is applied to (34)–(41), the control-to-output transfer function can be defined and derived

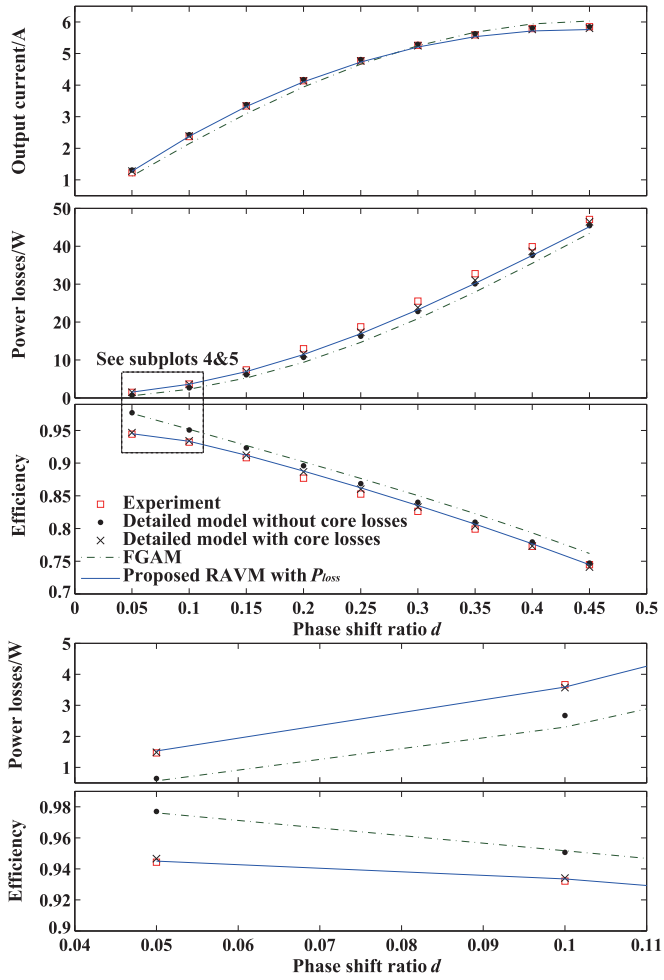

Fig. 9. Output current, power losses, and efficiency predictions compared to the actual measurements, with $V_{is} = 41.5$ V and $V_{os} = 20$ V.

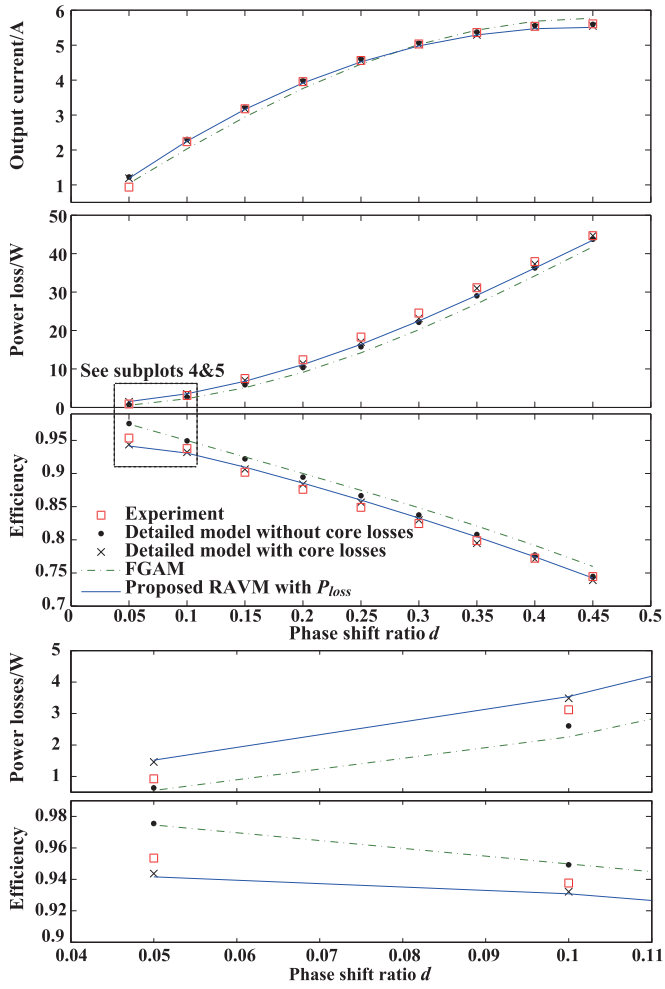

Fig. 10. Output current, power losses, and efficiency predictions compared to the actual measurements, with $V_{is} = 40$ V and $V_{os} = 20$ V.

as

$$G_{od}(s) = \left.\frac{\hat{i}_2(s)}{\hat{d}(s)}\right|_{\hat{v}_{is}(s)=0,\hat{v}_{os}(s)=0} = \frac{1}{R_o + L_2 s} \cdot \frac{x - yp/G_{A1}(s)}{nG_{A2}(s) + yr/G_{A1}(s)}, \quad (48)$$

where

$$G_{A1}(s) = (1/R_1 + C_1 s) + \frac{1}{L_1 s} + q - \frac{1/R_1}{1 + R_1 C_2 s} \quad (49)$$

and

$$G_{A2}(s) = (1/R_2 + C_3 s) + \frac{1}{R_o + L_2 s} - \frac{z}{n} - \frac{1/R_2}{1 + R_2 C_4 s}. \quad (50)$$

Similarly, the control-to-input transfer function can be derived as

$$G_{id}(s) = \left.\frac{\hat{i}_1(s)}{\hat{d}(s)}\right|_{\hat{v}_{is}(s)=0,\hat{v}_{os}(s)=0} = \frac{1}{L_1 s} \cdot \frac{rx/G_{A2}(s) + pn}{nG_{A1}(s) + yr/G_{A2}(s)}. \quad (51)$$

V. Case Studies

The parameters of the DAB converter in this study are summarized in the Appendix. The detailed model of this DAB converter was implemented in PLECS, and the proposed RAVM and other models for comparison were implemented in MATLAB/Simulink. A prototype was built to verify the RAVM presented in this paper. The experimental DAB converter is designed for a back-up power application. Therein, the primary side of the converter is connected to a battery (V_{is}) with 40-to-48-V voltage. The secondary side is connected to a 20-V dc bus (V_{os}) through a cable. The peak current flowing to the dc bus is 5 A. In the experiment, the battery was imitated by a power supply, while the voltage bus was imitated by a power supply with a 7-A resistive load. To imitate the effect of the cable resistance on the dynamic response, we added the resistor $R_o = 0.5\ \Omega$ to the model and the prototype. When the model is applied to the real system, an actual R_o value should be use (it is generally much lower than $0.5\ \Omega$). The power stage of the experimental DAB converter (see Fig. 7) is composed of MOSFET switches (IPB144N12N3), a ferrite-core (E55/28/21) high-frequency transformer, and input/output filters. The turns

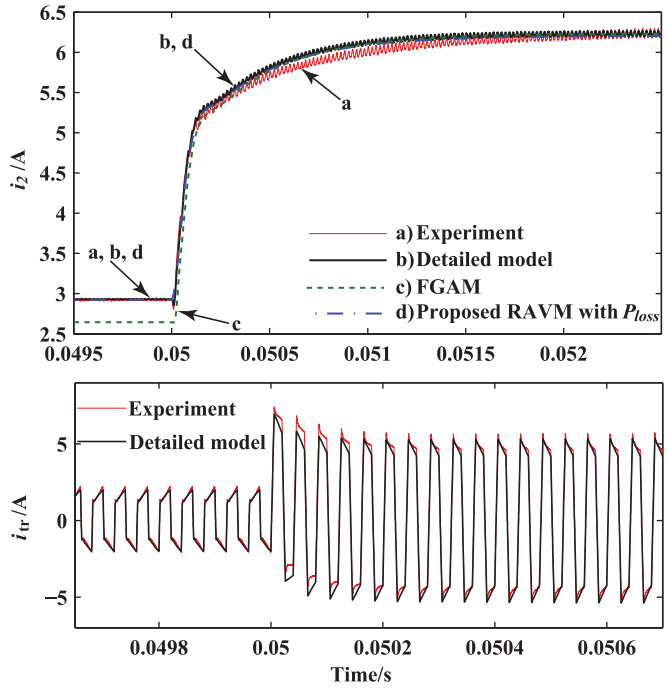

Fig. 11. Output current and transformer current transients with a phase shift change. Results are from the experimental measurement (thin solid line), the detailed model with core losses (thick solid line), FGAM (dashed line), and the proposed RAVM with power losses (dashed-dot line).

ratio of the primary to secondary windings is $40/20 = 2$. For the 100-W power rating, the leakage inductance $L_{eq} = 58$ μH is needed. Because the transformer in the prototype has a much lower (11.3 μH) leakage inductance, a 47-μH inductor is connected in series to the primary winding in order to increase the L_{eq} value. Consequently, as shown in Appendix, the inductance values $L_{l1} = 52.65$ μH and $L_{l2} = 1.41$ μH are used in the model. The control stage of the experimental DAB converter was implemented with a 32-bit floating-point microprocessor TMS320F28335 with 150-MHz clock.

In this section, in addition to experimental and detailed-modeling results, the following three available average models are discussed and compared:

1) the RAVM with an ideal transformer, i.e., no winding resistances or core losses (RAVM without P_{loss}), as defined in [27] and [28];
2) the full-order generalized average model (FGAM) only considering winding resistances, without core losses, as derived in [16];
3) the proposed RAVM with power losses, including conduction and core losses (the proposed RAVM with P_{loss}).

A. Power Loss Analysis

The model steady-state predictions and the experimental results are compared in Figs. 8–10. Specifically, the input current, the power losses, and the efficiency of the DAB converter with different phase shift ratios are plotted. In the models and the prototype, V_{os} is set as 20 V, while V_{is} is set as various values. Figs. 8–10, respectively, show the plots of the DAB converter with $V_{is} = 48$ V, 41.5 V, and 40 V. The data shown in each subplot include the experimental measurement and predictions from the detailed model without core losses, the detailed model with core losses, and the two average models (FGAM and proposed RAVM with P_{loss}). Considering the inside impedance of the secondary power source, the power loss P_{loss} is calculated through

$$P_{loss} = V_{in} \cdot i_1 - v_o \cdot i_2 \tag{52}$$

$$V_{in} = V_{is} \tag{53}$$

$$v_o = V_{os} + i_2 \cdot R_o \tag{54}$$

where the variables are defined in Fig. 4. As seen in Figs. 8–10, the prediction error from the proposed RAVM is generally small with respect to the experimental results, because the proposed RAVM includes the majority of power losses in the circuit. As shown in the magnified subplots 4 and 5, if R_M is not considered, there is a significant mismatch between the experimental results and model predictions of power losses and the efficiency, especially, when d is small. This is because the core loss of the transformer becomes more noticeable with respect to the total power conversion when d is small. Moreover, it is observed that the proposed RAVM with power losses has better accuracy in predicting the efficiency and power losses than FGAM. This is because FGAM does not include R_M, and this model is built based on first harmonic only so that its accuracy will deteriorate when harmonic distortions are higher [32], [33]. Moreover, in general, the prototype has slightly higher power losses than the model predictions due to the existence of unpredicted conduction losses on wires and PCB.

It is noted that DAB converters are commonly operating in zero-voltage-switching (ZVS) mode, and therefore, the switching loss is not considered in this study, as emphasized in Section I. When the DAB converter is operating in non-ZVS mode, the accuracy of the proposed RAVM becomes lower. For an ideal DAB without parasitic resistances, $V_{is}n : V_{os} = 1$ should be ensured in order that ZVS operation can be achieved with a wide range of d values [36]. In the prototype, due to the existence of R_{eq} and R_o, the actual voltage ratio of the DAB is lower than $V_{is} : V_{os}$. For this reason, ZVS operation is achievable when $V_{is}n : V_{os}$ is slightly higher than 1 in the experiment. Specifically, ZVS operation is achieved when $V_{is} = 40$–48 V and $d = 0.05$–0.45 except $V_{is} = 40$ or 48 V and $d = 0.05$. With $V_{is} = 40$ or 48 V and $d = 0.05$, ZVS operation is not completely achieved. In this case, the proposed RAVM cannot offer an accurate prediction. This results in a distinct mismatch between predictions and measurements of the output current. In other conditions, it is observed that the measurements highly match the predictions from the proposed RAVM with power losses.

B. Open-Loop Dynamic Response

In this study, the converter is assumed to initially operate under $d = 0.1$; at $t = 0.05$ s, the control variable d is increased from 0.1 to 0.3. As shown in Fig. 11, the output current i_2 and the transformer current i_{tr} are rising at that time, which is caused by the increased phase shift ratio. As observed in Fig. 11, the

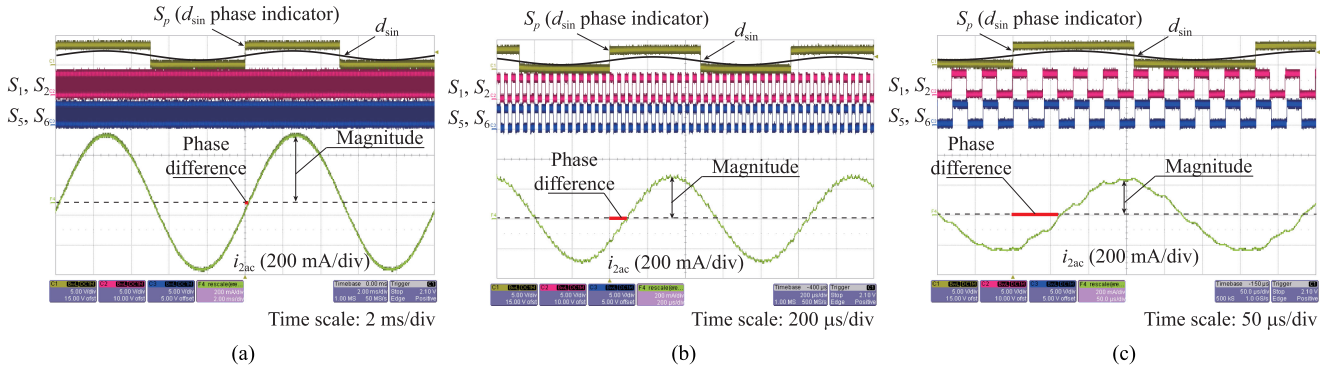

Fig. 12. Illustration of frequency-response measurements with $D = 0.1$ and various f_p values: (a) $f_p = 100$ Hz, (b) $f_p = 1.04$ kHz, and (c) $f_p = 3.125$ kHz.

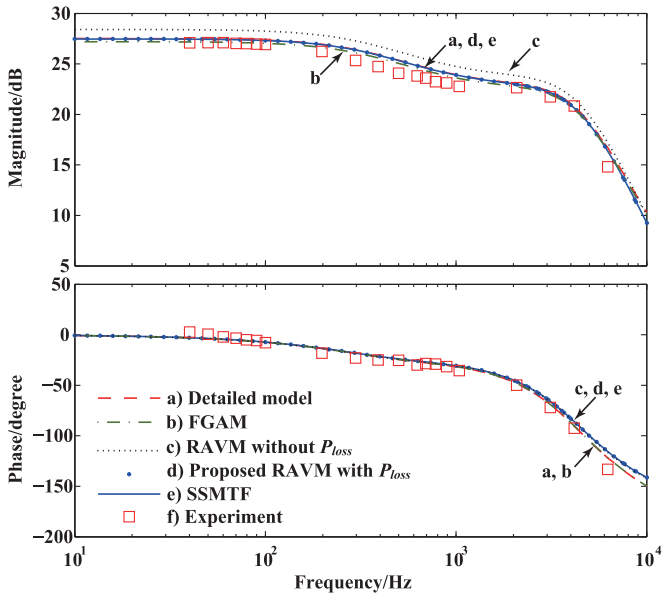

Fig. 13. Bode plots of control-to-output transfer functions with $D = 0.1$. Results are from the detailed model with core losses (dashed line), FGAM (dashed-dot line), RAVM without power losses (dotted line), the proposed RAVM with power losses (dots), the analytical prediction based on the proposed RAVM SSMTF (solid line), and experimental measurements (square markers).

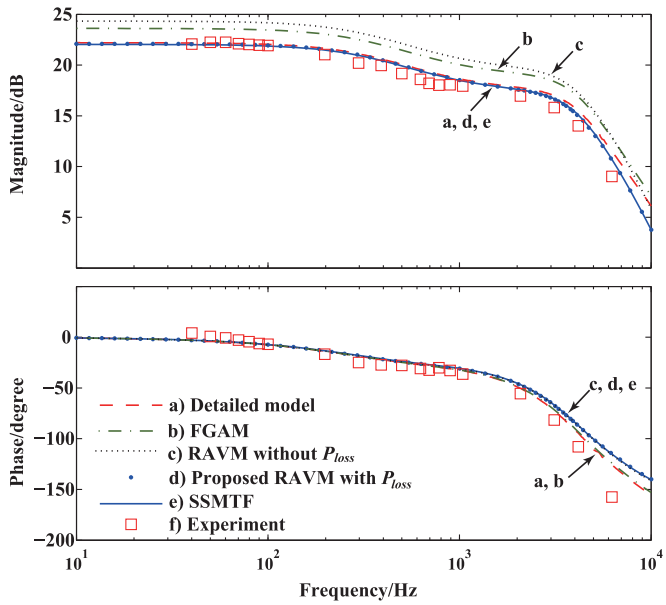

Fig. 14. Bode plots of control-to-output transfer functions with $D = 0.25$.

proposed RAVM and the detailed model match the experimental results extremely well. A small mismatch between these two models and the experimental results are mainly due to the higher-order parasitics in the actual circuit (series resistance from skin effects, parasitic capacitances, etc.) which are not considered in the modeling. The errors in the output current predicted by the FGAM are larger when $d = 0.1$, since the transformer current contains more harmonics under this condition.

C. Frequency-Domain Analysis

In this section, the frequency-domain analyses are separately performed using various models at quiescent operating points with $D = 0.1$, 0.25, and 0.4. In these models, $V_{is} = 48$ V and $V_{os} = 20$ V. The analyses are also verified by the experimental measurements.

First, a control-to-output transfer function in small-signal sense is extracted from the detailed model using PLECS toolbox. The same transfer function is then obtained from the three average models using MATLAB/Simulink. Additionally, one more result is derived using the analytical expression (48) for the small-signal model transfer function (SSMTF). In the experiment, a small perturbation $d_{\sin}$ is added to the quiescent point of the phase shift ratio D. Then, the actual phase shift ratio becomes a function of time t, namely

$$d(t) = D + d_{\sin}(t), \quad d_{\sin}(t) = A_m \sin 2\pi f_p t \tag{55}$$

where $A_m = 0.02$ is the amplitude and f_p ranging from 40 Hz to 6.25 kHz is the frequency of the perturbation $d_{\sin}$. Note that the d level cannot be continuously changed in the experiment, because there is a 6.67-ns minimum time resolution for time counters of the digital controller. This implies that the minimum variation of d is $\Delta d_{\min} = 6.67$ ns/20 μs $= 3.33 \times 10^{-4}$. When A_m is set as 0.02, d may have a $2A_m/\Delta d_{\min} = 120$-level resolution for the variation of $d_{\sin}$. This resolution is sufficient for our measurement. The frequency-response measurement is illustrated by Fig. 12. The magnitude response is obtained by

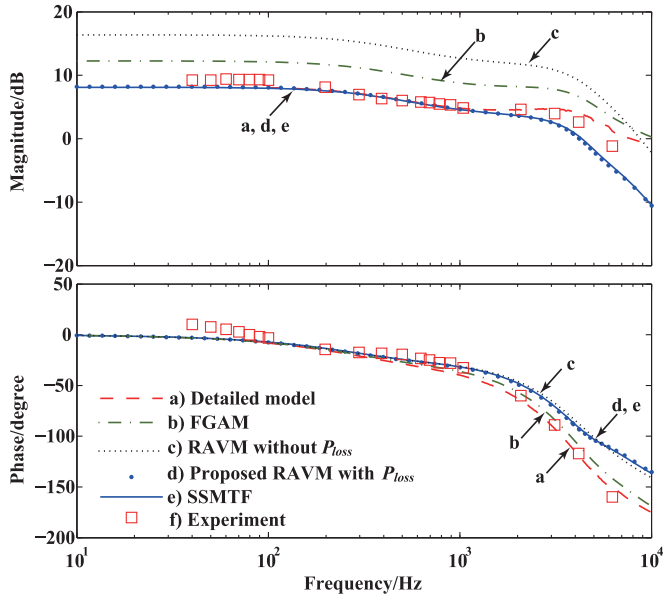

Fig. 15. Bode plots of control-to-output transfer functions with $D = 0.4$.

measuring the peak value of i_2 waveforms. The phase response is obtained by measuring the phase difference between the ac part of i_2 and the $d_{\sin}$ signal which is indicated by a square-wave signal S_p.

The comparisons of bode plots obtained from the experiment and models are shown in Figs. 13–15. When $D = 0.1$, there is no significant difference among the results from the proposed RAVM with power losses, FGAM, the detailed model, and the experiment. When $D = 0.25$ or 0.4, the proposed RAVM achieves more accurate predictions in low frequency. The difference between the results from the proposed RAVM and the detailed model (or the experiment) gradually increases with the frequency. Specifically, with $D = 0.25$, a distinct difference appears when $f_p > 5$ kHz (see Fig. 14), whereas with $D = 0.4$, that appears when $f_p > 2.5$ kHz (see Fig. 15). In general, FGAM achieves more accurate phase-response predictions than the proposed RAVM in high frequency (particularly when $D = 0.25$ or 0.4) because of its high-order property. However, the accuracy of magnitude response prediction from FGAM is significantly lower than that from the proposed RAVM. These are the pros and cons of full-order models. As compared with full-order models, the existing RAVM without power losses has a lower accuracy, especially in magnitude. However, the proposed RAVM with power losses does not have this deficiency while offering great simplicity.

VI. Conclusion

This paper presents a new RAVM for DAB converters, which requires much less computations than detailed models. The proposed approach considers major power losses (including conduction and transformer power losses) as well as the input/output filters. Based on the large-signal RAVM, the small-signal model and the control-to-output transfer function are also derived. This derivation also shows that Taylor series method may be used very effectively for analytical linearization of the RAVMs. The proposed RAVM is compared with the FGAM and the detailed model in predicting large-signal transients and small-signal analysis in the frequency domain, and demonstrated to offer very good accuracy. In particular, as compared with the previously established RAVM without power losses and FGAM, the proposed RAVM with power losses provides more accurate results in predicting the overall power losses and the efficiency, which may be very useful for system-level studies.

Appendix

$C_1 = 44\ \mu$F, $C_2 = 180\ \mu$F, $C_3 = 94\ \mu$F, $C_4 = 330\ \mu$F,
$L_1 = 15\ \mu$H, $L_2 = 22\ \mu$H, $L_{l1} = 52.65\ \mu$H, $L_{l2} = 1.41\ \mu$H, $L_M = 1.4$ mH,
$R_1 = 0.68\ \Omega$, $R_2 = 0.68\ \Omega$, $R_o = 0.5\ \Omega$,
$R_{l1} = 0.64\ \Omega$, $R_{l2} = 0.16\ \Omega$, $R_s = 0.0147\ \Omega$, $R_M = 2000\ \Omega$,
$f_s = 25$ kHz, $n = 0.5$.

References

[1] L. Zhu, "A novel soft-commutating isolated boost full-bridge ZVS-PWM DC–DC converter for bidirectional high power applications," *IEEE Trans. Power Electron.*, vol. 21, no. 2, pp. 422–429, Mar. 2006.
[2] H. Xiao and S. Xie, "A ZVS bidirectional DC–DC converter with phase-shift plus PWM control scheme," *IEEE Trans. Power Electron.*, vol. 23, no. 2, pp. 813–823, Mar. 2008.
[3] M. H. Kheraluwala, R. W. Gascoigne, D. M. Divan, and E. D. Baumann, "Performance characterization of a high-power dual active bridge dc-to-dc converter," *IEEE Trans. Ind. Appl.*, vol. 28, no. 6, pp. 1294–1301, Nov./Dec. 1992.
[4] H. Bai and C. Mi, "Eliminate reactive power and increase system efficiency of isolated bidirectional dual-active-bridge DC–DC converters using novel dual-phase-shift control," *IEEE Trans. Power Electron.*, vol. 23, no. 6, pp. 2905–2914, Nov. 2008.
[5] B. Hai, C. Mi, and S. Gargies, "The short-time-scale transient processes in high-voltage and high-power isolated bidirectional dc-dc converters," *IEEE Trans. Power Electron.*, vol. 23, no. 6, pp. 2648–2656, Jun. 2008.
[6] R. De Doncker, D. Divan, and M. Kheraluwala, "A three-phase soft-switched high-power-density dc/dc converter for high-power applications," *IEEE Trans. Ind. Appl.*, vol. 27, no. 1, pp. 63–73, Jan./Feb. 1991.
[7] S. Bhattacharya *et al.*, "Design and development of generation-I silicon based solid state transformer," in *Proc. IEEE Appl. Power Electron. Conf. Expo.*, 2010, pp. 1666–1673.
[8] J. Shi, W. Gou, H. Yuan, T. Zhao, and A. Huang, "Research on voltage and power balance control for cascaded modular solid-state transformer," *IEEE Trans. Power Electron.*, vol. 26, no. 4, pp. 1154–1166, Apr. 2011.
[9] S. Inoue and H. Akagi, "A bidirectional isolated dc-dc converter as a core circuit of the next-generation medium-voltage power conversion system," *IEEE Trans Power Electron.*, vol. 22, no. 2, pp. 535–542, Feb. 2007.
[10] B. Zhao, Q. Song, W. Liu, and Y. Xiao, "Next-generation multi-functional modular intelligent UPS system for smart grid," *IEEE Trans. Ind. Electron.*, vol. 60, no. 9, pp. 3602–3618, Sep. 2013.
[11] F. Krismer and J. Kolar, "Accurate power loss model derivation of a high-current dual active bridge converter for an automotive application," *IEEE Trans Ind. Electron.*, vol. 57, no. 3, pp. 881–891, Mar. 2010.
[12] A. Alonso, J. Sebastian, D. Lamar, M. Hernando, and A. Vazquez, "An overall study of a dual active bridge for bidirectional dc/dc conversion," in *Proc. IEEE Energy Convers. Cong. Expo.*, 2010, pp. 1129–1135.
[13] C. Mi, H. Bai, C. Wang, and S. Gargies, "Operation, design and control of dual H-bridge-based isolated bidirectional dc-dc converter," *IET Power Electron.*, vol. 1, no. 4, pp. 507–517, Apr. 2008.
[14] S. Dutta and S. Bhattacharya, "Predictive current mode control of single phase dual active bridge DC to DC converter," in *Proc. IEEE Energy Convers. Cong. Expo.*, 2013, pp. 5526–5533.
[15] H. Wen and W. Xiao, "Bidirectional dual-active-bridge DC-DC converter with triple-phase-shift control," in *Proc. IEEE Appl. Power Electron. Conf. Expo.*, 2013, pp. 1972–1978.

[16] H. Qin and J. W. Kimball, "Generalized average modeling of dual active bridge DC-DC converter," *IEEE Trans. Power Electron.*, vol. 27, no. 4, pp. 2078–2084, Apr. 2012.
[17] R. T. Naayagi, A. J. Forsyth, and R. Shuttleworth, "High-power DCDC converter for aerospace applications," *IEEE Trans. Power Electron.*, vol. 27, no. 11, pp. 4366–4379, Nov. 2012.
[18] A. Jain and R. Ayyanar, "PWM control of dual active bridge: Comprehensive analysis and experimental verification," *IEEE Trans. Power Electron.*, vol. 26, no. 4, pp. 1215–1227, Apr. 2011.
[19] S. A. Akbarabadi, M. Sucu, H. Atighechi, J. Jatskevich, "Numerical average value modeling of second order flyback converter in both operational modes," in *Proc. IEEE Workshop Control Model. Power Electron.*, 2013, pp. 1–6.
[20] A. Davoudi, J. Jatskevich, and P.L. Chapman, "Averaged modelling of switched-inductor cells considering conduction losses in discontinuous mode," *IET Electr. Power Appl.*, vol. 1, no. 3, pp. 402–406, May 2007.
[21] Y. Xie, J. Sun, and J. S. Freudenberg, "Power flow characterization of a bidirectional galvanically isolated high-power dc/dc converter over a wide operating range," *IEEE Trans. Power Electron.*, vol. 25, no. 1, pp. 54–66, Jan. 2010.
[22] G. W. Wester and R. D. Middlebrook, "Low-frequency characterization of switched dc–dc converters," *IEEE Trans. Aerosp. Electron. Syst.*, vol. AES-9, no. 3, pp. 376–385, May 1973.
[23] F. Krismer and J. W. Kolar, "Accurate small-signal model for the digital control of an automotive bidirectional dual active bridge," *IEEE Trans. Power Electron.*, vol. 24, no. 12, pp. 2756–2768, Dec. 2009.
[24] R. D. Middlebrook and S. Ćuk, "A general unified approach to modelling switching-converter power stages," in *Proc. IEEE Power Electron. Spec. Conf.*, 1976, pp. 18–34.
[25] R. W. Erickson and D. Maksimovic, *Fundamentals of Power Electronics*, 2nd ed. New York, NY, USA: Springer-Verlag, 2001.
[26] H. K. Krishnamurthy and R. Ayyanar, "Building block converter module for universal (ac–dc, dc–ac, dc–dc) fully modular power conversion architecture," in *Proc. IEEE Power Electron. Spec. Conf.*, 2007, pp. 483–489.
[27] H. Bai, M. Chunting, W. Chongwu, and S. Gargies, "The dynamic model and hybrid phase-shift control of a dual-active-bridge converter," in *Proc. IEEE Ind. Electron. Conf.*, 2008, pp. 2840–2845.
[28] H. Bai, Z. Nie, and C. C. Mi, "Experimental comparison of traditional phase-shift, dual-phase-shift, and model-based control of isolated bidirectional dc-dc converters," *IEEE Trans. Power Electron.*, vol. 25, no. 6, pp. 1444–1449, Jun. 2010.
[29] D. Costinett, "Reduced order discrete time modeling of ZVS transition dynamic in the dual active bridge converter," in *Proc. IEEE Appl. Power Electron. Conf. Expo.*, 2015, pp. 365–370.
[30] B. Farhangi, H. A. Toliyat, "Piecewise linear model for snubberless dual active bridge commutation," *IEEE Trans. Ind. Appl.*, vol. 51, no. 5, pp. 4072–4078, Sep./Oct. 2015.
[31] C. Zhao, S. D. Round, and J. W. Kolar, "Full-order averaging modelling of zero-voltage-switching phase-shift bidirectional dc-dc converters," *IET Power Electron.*, vol. 3, no. 3, pp. 400–410, 2010.
[32] J.-R. Sibue, J.-P. Ferrieux, G. Meunier, R. Périot, and E. Clavel, "Generalized average model of series–parallel resonant converter with capacitive output filter for high power application," 2010. [Online]. Available: https://hal.archives-ouvertes.fr/hal-00521993
[33] J. M. Ramos, J. Diaz, A. M. Pernía, F. Nuño, and J. M. Lopera, "Dynamic and steady-state models for the PRC-LCC resonant topology with a capacitor as output filter," *IEEE Trans. Ind. Electron.*, vol. 54, no. 4, pp. 2262–2275, Aug. 2007.
[34] B. Zhao, Q. Song, W. Liu, G. Liu, and Y. Zhao, "Universal high-frequency-link characterization and practical fundamental-optimal strategy for dual-active-bridge DC-DC converter under PWM plus phase-shift control," *IEEE Trans. Power Electron.*, vol. 30, no. 12, pp. 6488–6494, Dec. 2015.
[35] B. Zhao, Q. Yu, and W. Sun, "Extended-phase-shift control of isolated bidirectional DC–DC converter for power distribution in microgrid," *IEEE Trans. Power Electron.*, vol. 27, no. 11, pp. 4667–4680, Nov. 2012.
[36] A. Rodríguez, A. Vázquez, D. G. Lamar, M. M. Hernando, and J. Sebastin, "Different purpose design strategies and techniques to improve the performance of a dual active bridge with phase-shift control," *IEEE Trans. Power Electron.*, vol. 30, no. 2, pp. 790–804, Feb. 2015.

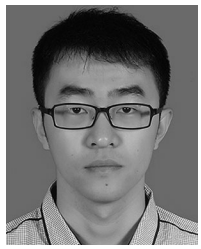

Kai Zhang received the B.Eng. degree from the Huazhong University of Science and Technology, Wuhan, China, in 2013, and the M.A.Sc. degree from the University of British Columbia, Vancouver, BC, Canada, in 2015.

He is currently with Guangzhou Power Supply Co. Ltd., China Southern Power Grid Co. Ltd., Guangzhou, China. His research interests include analysis and modeling of dc–dc converters.

Zhenyu Shan (S10–M'13) received the B. Eng. and M.Eng. degrees in control engineering from Beijing Jiaotong University, Beijing, China, in 2007 and 2009, respectively, and the Ph.D. degree in power electronics from Hong Kong Polytechnic University, Hong Kong, in 2013.

Supported by the Ph.D. Student Attachment Program of the university, he was a Visiting Student at the Grainger Center for Electric Machinery and Electromechanics, University of Illinois at Urbana-Champaign, Champaign, IL, USA, from March to June 2013. He has been a Postdoctoral Fellow with the Department of Electrical and Computer Engineering, University of British Columbia, Vancouver, BC, Canada, since November 2013. His research interests include converter-based ac–dc systems, computer power supply design, and power converter modeling and nonlinear control.

Dr. Shan serves as a Reviewer for various IEEE transactions and other international journals on electrical and electronic engineering.

Juri Jatskevich (M'99–SM'07) received the M.S.E.E. and Ph.D. degrees in electrical engineering from Purdue University, West Lafayette IN, USA, in 1997 and 1999, respectively.

Since 2002, he has been a Faculty Member at the University of British Columbia, Vancouver, BC, Canada, where he is currently a Professor of electrical and computer engineering. His research interests include power electronic systems, electrical machines and drives, modeling, and simulation of electromagnetic transients.

Dr. Jatskevich has served as an Associate Editor for the IEEE TRANSACTIONS ON POWER ELECTRONICS for the period 2008–2013 and is currently the Editor-In-Chief of the IEEE TRANSACTIONS ON ENERGY CONVERSION, and an Editor of the IEEE POWER ENGINEERING LETTERS. He Chaired the IEEE CAS Power Systems and Power Electronic Circuits Technical Committee in 2009–2010. He is also chairing the IEEE Task Force on Dynamic Average Modeling, under Working Group on Modeling and Analysis of System Transients Using Digital Programs. He was the General Chair of the Sixteenth IEEE Workshop on Control and Modeling for Power Electronics (COMPEL 2015), and he presently also serves on the IEEE Publication Services and Products Board (PSPB) Strategic Planning Committee, IEEE PELS Power and Control Core technologies and IEEE PES Electric Machinery Committee.